Composites: Part A 79 (2015) 23–29

Contents lists available at ScienceDirect

Composites: Part A

journal homepage: www.elsevier.com/locate/compositesa

Three-dimensional imaging and quantitative analysis of dispersion and mechanical failure in filled nanocomposites

Benjamin E. Smith [a,*], Hessam Yazdani [b], Kianoosh Hatami [b]

[a] Samuel Roberts Noble Microscopy Laboratory, University of Oklahoma, Norman, OK 73019, USA
[b] School of Civil Engineering and Environmental Science, University of Oklahoma, Norman, OK 73019, USA

ARTICLE INFO

Article history:
Received 17 June 2015
Received in revised form 13 August 2015
Accepted 15 August 2015
Available online 24 August 2015

Keywords:
A. Nanocomposites
B. Mechanical properties
D. Non-destructive testing
Optical microscopy

ABSTRACT

Characterizing filled nanocomposites is an active area of research in order to predictively modify their properties. The dispersion of nanofillers has a direct influence on these properties, and therefore the precise characterization of dispersion is essential in establishing a complete understanding of composite behavior. In this study, we have developed a methodology for using laser scanning confocal microscopy to quantitatively assess the three-dimensional dispersion of carbon nanotube bundles within a composite material *in situ*. Furthermore, we applied this methodology to directly visualize in real-time the subsurface mechanical failure of a carbon nanotube-filled composite.

1. Introduction

Dispersing a sufficient quantity of nanofillers such as nanoclays [1], nano-oxides [2], metal nanopowders [3], carbon blacks [4], graphene [5] and carbon nanotubes (CNTs) [6] into a polymer matrix results in a composite that typically offers improved properties compared to the host polymer in pristine form. The extent of improvement, however, depends not only on the concentration of the filler but also its dispersion quality, aggregation tendency and alignment distribution.

For nanocomposite materials, the term dispersion generally refers to the distribution of individual fillers in a matrix. However, this definition needs to be adjusted for nanocarbons (e.g. CNT and graphene) that possess an inherent thermodynamic drive to create physical entanglement with neighboring particles via van der Waals forces and form an aggregated morphology called bundles [7]. Therefore, a dispersion state considered as "uniform" or "good" for nanocarbons in the nanoscale does not necessarily reflect the dispersion state at the micro- and macroscales. This distinction is especially important when predicting a particular property of a composite, which requires an understanding of filler dispersion at different length scales [8].

While there have been significant advances in the homogeneous dispersion of nanocarbons in polymers (e.g. see a review by Ma et al. [8] for CNTs), there are currently limited methodologies for quantifying the dispersion state of these fillers at different length scales. Measuring the percolation threshold is a common technique to semiquantitatively probe the state of nanoscopic dispersion in polymers, which is defined as the minimum concentration of conductive particles required to create a continuous interconnecting network of particles that results in an abrupt insulator-to-(quasi)conductor transition [9]. However, a higher percolation threshold filler can have significantly better dispersion than a lower percolation threshold filler as bundling can reduce the percolation threshold [10]. As such, nanoscopic and microscopic visualization techniques are an essential means toward a deeper and more direct insight into the nature of aggregate dispersion in filled composites.

Different techniques such as atomic force, scanning and transmission electron microscopy (AFM, SEM and TEM, respectively) have been used to visualize inclusions at different length scales.

AFM, which collects images of a specimen surface by moving a probe over that surface in a raster scan pattern, provides images with a resolution on the order of fractions of a nanometer, allowing the visualization of the objects as small as individual CNTs [11]. However, its application is limited to surface imaging, and its relatively slow rate of scanning results in thermally drift-distorted images that need to be corrected using enhancement techniques [12].

SEM, in contrast, scans a specimen with a focused beam of electrons. A particular SEM imaging mode named the charge-contrast SEM imaging allows the 3D construction of the microstructure of a specimen to a depth of up to one micron. In this mode,

* Corresponding author.
E-mail address: benjamin.smith@ou.edu (B.E. Smith).

http://dx.doi.org/10.1016/j.compositesa.2015.08.019
1359-835X/

microscopic objects charged by a high-accelerating voltage are visible due to emitting enriched secondary electrons [13]. Zhao et al. [14] recently used this imaging mode combined with stereo imaging to obtain a several-hundred-nm deep 3D view into the microstructure of CNT–polyimide composites. However, a disadvantage of using this mode is that insulating materials such as polyimide or polyvinyl chloride (PVC) undergo a charge buildup when exposed to high-voltage electrons. Consequently, at too high of a voltage a threshold contrast is not produced and the conductive filler cannot be distinguished from the noise of background fluctuations and the insulating matrix, yielding low-resolution images.

TEM forms images from the interaction of a beam of electrons passing through an ultra-thin specimen. It can provide very high-resolution images to a scale of 0.2 nm and has proven particularly effective in measuring the average bundle size, as well as bundle density. Since sections are at most tens of nm thick, there is not much depth information within one section. Serial thin sectioning (also known as TEM tomography) resolves this issue by aligning the images of a great number of thin sections. However, the 3D reconstruction of a specimen hundreds of microns thick using this technique would require a prohibitively-laborious procedure to obtain hundreds to thousands sections and align their images [15].

Other techniques such as scanning acoustic microscopy and particle-sizing methods are not suitable to characterize the morphological features of CNT-filled polymer composites. Scanning acoustic microscopy, which uses short high-frequency acoustic pulses to scan a specimen on a millimeter scale, is not well-suited for polymers due to the significant attenuation of ultrasonic waves in viscoelastic materials that limits the penetration depth [16]. Particle-sizing methods such as laser diffractometry, which are based the assumption that the filler particles are primarily spherical in shape, have been shown to be inaccurate in determining the size of extremely non-spherical particles such as CNTs in suspension form before they are embedded in a polymer matrix [17]. Furthermore, laser diffractometry requires that the light is able to travel through the entire sample, which can pose a problem with carbon based nanocomposites due to carbon's substantial light absorption in the visible spectrum. Additionally, diffractiometry lacks positional information of the aggregates within the sample. The survey above demonstrates the technical limitations and difficulties involved in using the microcopy techniques described for the subsurface imaging (also known as depth profiling) of filled composites.

Laser scanning confocal microscopy (LSCM) is a light microscopy technique which creates 3D reconstructions, with up to 300 nm resolution. In conventional microscopes, the light is transmitted through the entire specimen thickness, requiring that the sample is capable of transmitting light, and that bundles do not obscure one another. LSCM circumvents this limitation by utilizing light in the reflected light path, while also blocking any out-of-focus light, creating an image as thin as 300 nm axially, referred to as an optical section. By collecting a series of optical sections along the optical axis (*Z*-axis), one can generate a 3D reconstruction of a volume within an intact specimen.

Previous studies have used LSCM to assess 3D nanofiller dispersion by looking at direct laser reflection off of CNT bundles in poly(methyl methacrylate) [18]. While reflected light LSCM can give an approximate 3D image, it has several limitations when it comes to assessing 3D dispersion. First, only surfaces that are approximately perpendicular to the objective will reflect light back into the objective. This means that steeply inclined portions of a bundle surface, and the entire back side of the bundle are not visible with this technique. Additionally, bundles closest to the objective will obscure bundles deeper in the material, resulting in an underestimation of bundle density deeper within the specimen.

In order to address the limitations of the above methods, we report the development of a practical LSCM technique for the rapid 3D characterization of the dispersion and distribution of CNT bundles *in situ* using host polymer autofluorescence. Additionally, with the use of a manual tensioning stage, we were able to apply our method to characterize the subsurface failure mechanism of a CNT filled nanocomposite. Non-autofluorescent materials could also benefit from this technique by incorporating trace amounts of a fluorescent dye into the host polymer.

2. Methods

2.1. Materials and sample fabrication

PVC plastisol was used as the host polymer for the composites investigated in this study. A multi-walled CNT (MWCNT) with the properties as given in Table 1 was used as the filler. An auxiliary plasticizer (bis(2-ethylhexyl) phthalate) was used to lower the melt viscosity of the composite. The MWCNT was first dispersed into the plasticizer at a weight ratio of 1:24 using a probe sonicator operating at a power of 55 W for a net duration of 60 min using a 50% pulse mode. The ratio was determined as per the viscosity and processablity requirements in the geosynthetics industry. The resulting blended material was subsequently mixed with the plastisol at a ratio of 1:7 to make samples filled with 0.5 wt.% MWCNT. This filler concentration corresponds to the upper bound of the percolation region of the composite where conductivity begins to plateau to a value a few orders of magnitude closer to that of the filler. Specifically, a conductivity of 3.4×10^{-9} S/m was measured for pure plastisol specimens (i.e. CNT% = 0), while the PVC composite filled with 0.5 wt.% MWCNT had a measured conductivity of $\approx 10^{-4}$ S/m. Subsequently, the composite was compression-molded using 1 MPa pressure at 180 °C for 15 min to fabricate samples for microscopy analysis. The pressure was sustained while the samples were allowed to cool down gradually to room temperature (typically, 23 °C) at a typical rate of 2.5 °C/min.

2.2. Transmission electron microscopy (TEM)

Samples were cryosectioned at 150 K (−123 °C) with a section thickness of ≈100 nm. The sections were mounted on 600 mesh hexagonal grids and imaged in bright field on a JEOL 2000FX transmission electron microscope at an accelerating voltage of 200 kV.

2.3. Laser scanning confocal microscopy (LSCM)

Test samples were imaged using a Leica SP8 laser scanning confocal microscope. The PVC was found to autofluoresce with UV excitation, so the samples were imaged using a 405 nm diode laser, and the emission intensity was measured between 446 nm and 554 nm.

High resolution 3D images of the CNT bundles were acquired using a 63 × 1.4 NA oil immersion objective. Oil immersion was chosen primarily because the refractive index of immersion oil, 1.52, is similar to that measured for PVC [20], helping to reduce optical aberrations that would otherwise compromise our resolution.

2.4. Imaging samples under tensile load

The samples were imaged under tensile strain using a modified tensioning microscope stage (Micro-Vice Holder, ST Japan–USA, LLC). Test samples were first loaded onto the vice at a starting length of 11.0 mm. The samples were then imaged via a series of

Table 1
Properties of the MWCNT used in this study (as measured, or provided by the supplier).

MWCNT supplier ID	Outer diameter (nm)	Length (μm)	Aspect ratio	Carbon purity (%)	D/G ratio from Raman	Surface area (m^2/g)	Density, ρ_f (g/cm^3)
SWeNT® SMW-100	7.8	74	95	>98	1.52	250	2.045

optical sections from the sample surface to 200 μm below the sample surface, measuring the UV excited autofluorescence with a 10 × 0.3 NA objective. The samples were then put under increasing tensile strain in 2.0 mm increments, and imaged at the same position at each increment, until sample failure. The pinhole aperture was opened to 6.00 Airy units to enable the use of a lower laser intensity, which helped to mitigate photobleaching while imaging. When tears within the material were observed, they were imaged in three dimensions by acquiring a series of optical sections in the Z direction with the pinhole aperture closed to 1.00 Airy units for better axial resolution.

High-resolution images of fractured CNT bundles were acquired on samples that had been pulled to failure. 3D images were acquired using a 63 × 1.4 NA oil immersion objective, imaging the UV excited autofluorescence.

2.5. Image processing and quantification

In order to better delineate the boundaries of the bundles in the high-resolution 3D images, the image series were deconvolved using an adaptive point-spread function over 10 iterations (AutoQuant X v3.0.3 64-bit) (Fig. 1b, Supplementary Fig. 1).

The boundary of each bundle was then determined by inverting the deconvolved image intensities (yielding bright bundles on a dark background) and then generating an isosurface within each image, delineating the bundles from the surrounding PVC (Imaris × 64 v8.0.1) (Fig. 1, Supplementary Movie 3), allowing for a quantitative 3D analysis of dispersion. The same isosurface threshold was used for every image to ensure that the samples were comparable.

The volume and position of each bundle within an image was quantified by measuring the volume and centroid of each isosurface within an image (Imaris × 64 v8.0.1). The distribution of bulk carbon within each image was measured by binarizing an image series, such that a voxel containing carbon had an intensity of 1 while PVC had an intensity of 0 (ImageJ v1.49 m). The percentage amount of the total volume of a 3D bin that was occupied by CNTs was calculated as:

$$\%\ total\ volume = \frac{\#\ of\ voxels\ containing\ CNTs}{total\ \#\ of\ voxels} \quad (1)$$

Statistical analysis and plotting was performed using R (R ×64 v3.1.2).

3. Results and discussion

CNTs are known to have high absorption in the UV range [21], which is also the wavelength we found that could efficiently excite autofluorescence in our host polymer, polyvinyl chloride (PVC). The absorption proved problematic when trying to image deep into composite samples, and especially when resolving the side of the CNT bundles opposite the objective. To resolve this issue, the samples were imaged starting 100 μm below the surface of the sample with a 27 μs exposure time per voxel, and were then imaged back toward the surface of the sample closest to the objective. The direction of the imaging resulted in photobleaching of the PVC closest to the objective giving a uniform image intensity, where the decreasing amount of UV absorption by the CNTs was offset by increasing photobleaching of the PVC as the sample was imaged closer to the surface (Fig. 1a, Supplementary Fig. 1). The total volume imaged for each test sample was 246 μm × 246 μm × 104 μm with a voxel dimension of 480 nm × 480 nm × 480 nm.

We were also able to detect autofluorescence from within the CNT bundles (Fig. 2a, Supplementary Movie 3), revealing that the CNT bundles were optically translucent rather than completely opaque. In order to confirm that the CNTs were organized in a manner to allow for the visualization of PVC within the composite, TEM was used to observe CNT composition within CNT bundles (Fig. 2b and c). We found that the bundles were a loose tangle of CNTs impregnated with PVC, confirming our observation of PVC fluorescence within the bundles via LSCM. Because of the translucent nature of the bundles, sufficient light was transmitted through the bundles for the full 3D structure of each bundle to be imaged via LSCM, including the side of the CNT bundles opposite the direction of illumination (Fig. 1, Supplementary Fig. 1).

Since the CNT bundles would have been stochastically sheared during sonication, we expected the volume distribution of the bundles to have a log-normal distribution [22], which has also been observed in previous studies of CNT dispersion by sonication [23]. A histogram of bundle volumes within our images confirmed a log-normal distribution (Fig. 3c, Supplementary Fig. 2a–c). Corresponding probability plots confirmed that the majority of

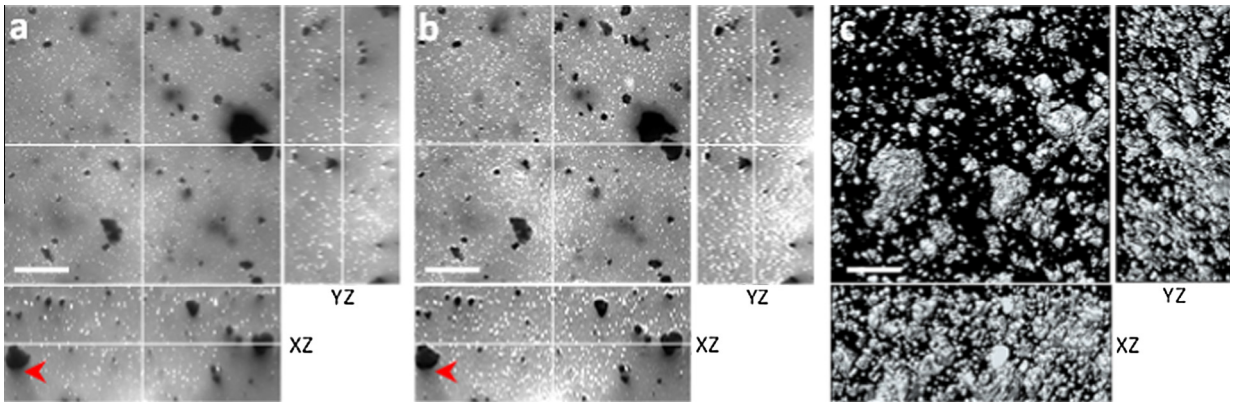

Fig. 1. 3D Imaging of CNT bundles. (a) Orthogonal sections from a 3D image of PVC autofluorescence in a CNT composite sample. The white lines show where the corresponding orthogonal sections are located in each image. The region immediately below the CNT aggregates was visible with only a slight shadow (arrowhead). (b) Image *a* post-deconvolution. The lower boundaries of the CNT bundles are more discrete (arrowhead). (c) Orthogonal views of the entire 3D image with an isosurface rendering around each bundle. Scale bars = 50 μm. (For interpretation of the references to colour in this figure legend, the reader is referred to the web version of this article.)

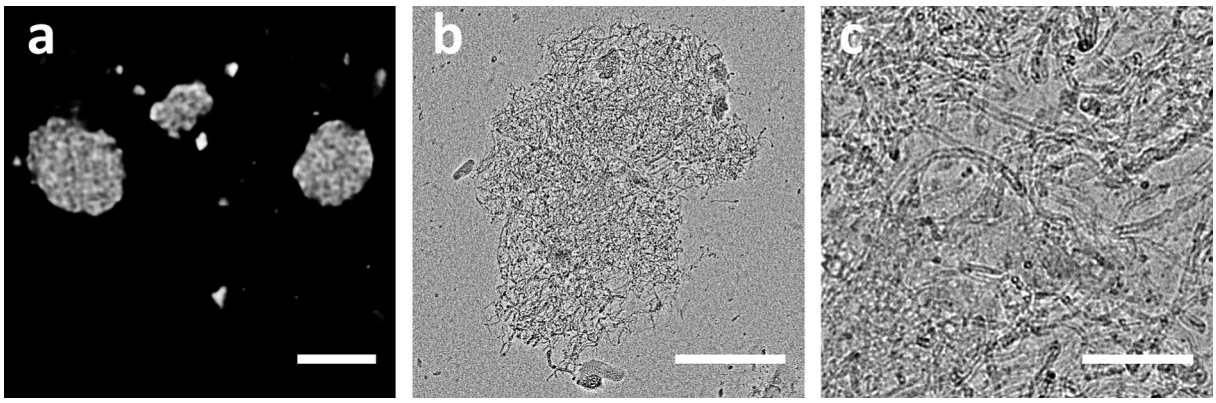

Fig. 2. CNT bundles are optically translucent with PVC impregnation into CNT bundles (a) a single optical section of a CNT bundle (white). PVC (black) is clearly visible within the bundle itself. Scale bar = 20 μm. (b) A TEM micrograph of a CNT bundle showing that the bundles are a loosely entangled cluster of CNTs impregnated with PVC. Scale bar = 1 μm. (c) A magnified view from *b*. Scale bar = 200 nm.

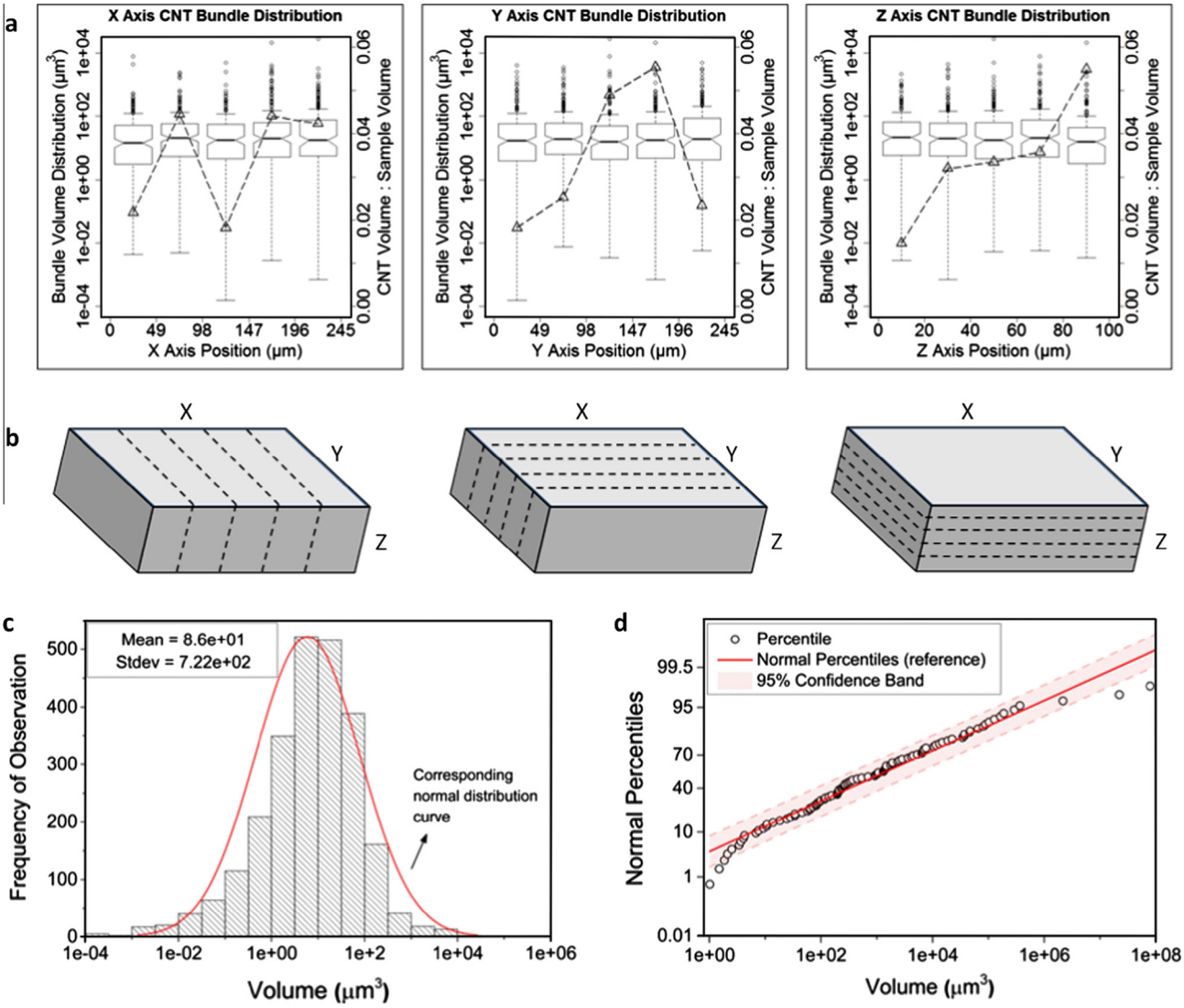

Fig. 3. Distribution of CNT bundles in PVC. (a) Plots showing the distribution of individual bundle volumes (box plots) as well as the bulk distribution of CNTs (dashed line) along the *X*, *Y* and *Z* axes of the image in Fig. 1. (b) A schematic showing how the total 3D image was divided into 5 bins along each axis in *a*, with the side of the image that was closest to the objective facing up. (c) Histogram of the distribution of the of bundle volumes, with the line showing the corresponding log-normal distribution. (d) Probability plot showing the distribution of bundle volumes relative to a log-normal distribution. Dashed lines = 95% confidence interval. (For interpretation of the references to colour in this figure legend, the reader is referred to the web version of this article.)

the bundle volumes were log-normally distributed with 95% confidence (Fig. 3d, Supplementary Fig. 2d–f). The probability plots also revealed that the distribution of bundle volumes below 1 μm^3 in volume were not normally distributed (Fig. 2d), which we expected as 1 μm^3 was the smallest volume we could accurately resolve given our voxel dimensions. Additionally, we tested for normality using the Kolmogorov–Smirnov test and the chi-square test, both of which verified the null hypothesis that the samples had a normal distribution.

Having validated our methodology for 3D quantitative imaging of the bundles within the sample, we then measured the spatial distribution of CNT bundles within the composite, determining if there was a positional dependence in bundle volume distribution and/or total carbon distribution. To answer this question, each image was divided into five equal bins along the *X*, *Y* and *Z* axes (Fig. 3b). The quality of dispersion was assessed through two different metrics. First, the distribution of the individual bundle volumes along each image axis was quantified (Fig. 3a, Supplementary Fig. 3 – box plot). Second, we measured the fraction of the total volume of each bin that was filled with CNT bundles (Fig. 3a, Supplementary Fig. 3 – line graph). While the distribution of bundle volumes was not significantly different throughout the sample, the bulk CNT content was dominated by the largest aggregates within the image, resulting in local concentrations in carbon content.

LSCM also offered a unique opportunity to observe the subsurface effects of tension on a composite material. Previous studies have assessed CNT nanocomposite material failure mechanisms based on the surface topology of strained samples via SEM [24,25] and LSCM [26,27]. The capacity of LSCM to image subsurface features also allows for monitoring the internal deformation of a composite sample while under a dynamic load [28]. Since our imaging method also allowed us to observe the CNT bundles up to 100 μm below the sample surface, we combined these techniques in our study by using LSCM to investigate both the surface topography as well as the subsurface CNT bundle deformation while the composite samples were under an increasing tensile load.

Specifically, dogbone test samples were loaded onto a tensioning microscope stage (Supplementary Fig. 4), and tightened until there was no slack in the sample (0% strain). The samples were then tensioned and imaged down to 200 μm below the surface of the material in 18% strain increments. We found that the largest CNT bundles fractured first between 18% and 36% strain (Fig. 4a, arrowhead, Supplementary Movie 1), which is close to the range of strain at failure reported for CNTs and graphene at room temperature (i.e. 8–20% [29,30]). As the tensile load increased, smaller bundles within the sample progressively fractured. Eventually, a single tear predominated at the surface, resulting in the mechanical failure of the sample (Supplementary Movie 1, arrowheads). In order to better understand the formation mechanism of these tears, we acquired 3D images of the tears that formed preceding the failure of the material (Fig. 4c). At the base of these tears, we found large, fractured bundles of CNTs (Fig. 4c, arrowhead). The polymer near the tear was also raised relative to the rest of the sample, suggesting that as the material began to fail, there was a resulting local reduction in stress. We then imaged six test samples in total at a different relative position each, and found that the sequential bundle rupturing occurred across the entire sample, independent of positon. The host polymer was also observed to have a low concentration of non-autofluorescent particles (Fig. 4a, Supplementary Movie 2); however, these particles did not fracture under tensile strain.

In order to study the exact nature of the bundle fractures, we performed high resolution 3D imaging of the CNT bundles after the test samples had been tensioned to failure (Fig. 4b, Supplementary Movie 4). Only bundles within ≈1 mm of the

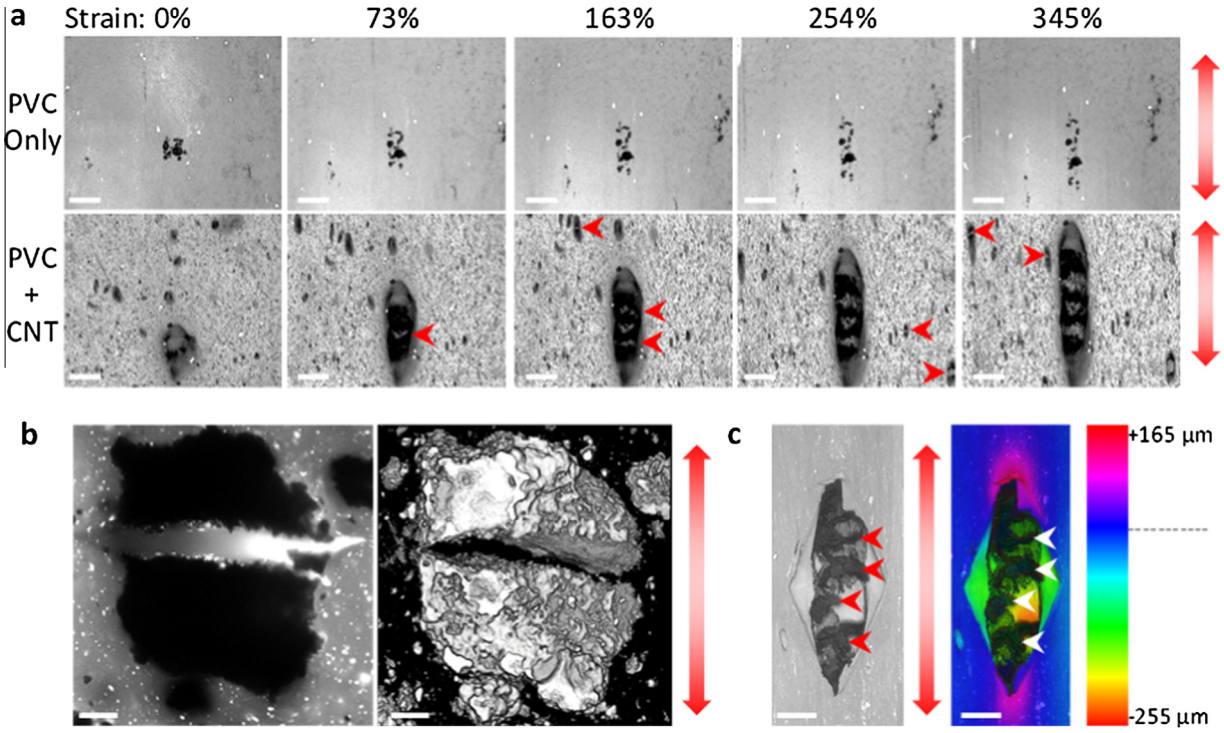

Fig. 4. Failure mechanics of the composite material under tensile strain. (a) Maximum intensity projections of test samples with and without CNTs under increasing strain. Arrowheads show where new fractures have formed within the CNT bundles. Scale bar = 200 μm. Arrows show direction of tensile loading. (b) A single optical section and 3D rendering of a fractured CNT bundle after tensile loading. Scale bar = 20 μm. (c) A 3D grayscale image and colorimetric surface profile of a large tear forming in a composite sample under tensile load, with a fractured CNT bundle clearly visible at the base of the tear (arrowhead). Scale bar = 200 μm. (For interpretation of the references to colour in this figure legend, the reader is referred to the web version of this article.)

failure site remained visibly fractured, and had ruptured perpendicular to the direction of tension, suggesting a brittle-like fracture. This observation was in agreement with previous studies that have also shown that increased CNT concentration within composite materials resulted in ductile host polymers becoming brittle [31].

This data collectively gives a potential model of how CNT bundles in ductile materials can lead to a localized failure of the material. Since the CNT bundles are local subregions of greatly increased CNT concentration, this causes the polymer/CNT composite to become locally brittle. As the tensile loading of the material leads to increased strain, stress becomes focused at the brittle CNT bundles, which ultimately fracture, with the largest bundles fracturing first, followed by smaller bundles. As tensile loading continues to increase, the host polymer proceeds to tear at the site of largest fracture(s), ultimately leading to the failure of the material.

We believe this serves to illustrate the capability of the imaging technique reported in this paper to further illuminate the influence of changes in the distribution of fillers and their subsequent rupture on the mechanical properties of nanocomposites. This microscopic information (i.e. the changes in interparticle/interbundle distances) could in turn be used to develop and validate models that are able to predict the properties (e.g. electrical resistance due to electron tunneling effects) of nanocomposites. Further applications could include improving carbon electromechanical actuators by observing their real-time microstructural changes due to temperature or a source of energy (e.g. electric current [32]). In addition, the technique could be utilized to explain the contradictory mechanical behaviors observed in CNT-filled composites made from different host polymers (e.g. [33]).

4. Conclusions

In this study, the subsurface images of CNT-filled PVC composites were used to demonstrate the capability of LSCM for quantitative imaging and detailed characterization of filled nanocomposites. This technique lays the foundation to precisely correlating specific dispersion metrics with desired composite properties and understanding their connection with the composite's microstructure. Additionally, due to the already wide availability of LSCM, this imaging technique could be readily adopted in an array of nanocomposite research studies, especially composites filled with particles of higher dimension (e.g. graphene).

Acknowledgments

The authors wish to thank Greg Strout, of the Samuel Roberts Noble Microscopy Laboratory, for his generous assistance with the transmission electron microscopy, including sample sectioning and imaging.

Appendix A. Supplementary material

Supplementary data associated with this article can be found, in the online version, at http://dx.doi.org/10.1016/j.compositesa.2015.08.019.

References

[1] Subramaniyan AK, Sun CT. Enhancing compressive strength of unidirectional polymeric composites using nanoclay. Compos Part Appl Sci Manuf 2006;37:2257–68. http://dx.doi.org/10.1016/j.compositesa.2005.12.027.
[2] Kang S, Mo Y, Ong SP, Ceder G. Nanoscale stabilization of sodium oxides: implications for Na–O_2 batteries. Nano Lett 2014;14:1016–20. http://dx.doi.org/10.1021/nl404557w.
[3] Bartolomé JF, Gutiérrez-González CF, Torrecillas R. Mechanical properties of alumina–zirconia–Nb micro–nano-hybrid composites. Compos Sci Technol 2008;68:1392–8. http://dx.doi.org/10.1016/j.compscitech.2007.11.010.
[4] Hatami K, Hassanikhah A, Yazdani H, Grady B. Tensoresistive PVC coating for sensor-enabled geogrids. J Nanomech Micromech 2014;4:A4013016. http://dx.doi.org/10.1061/(ASCE)NM.2153-5477.0000070.
[5] Rafiee MA, Rafiee J, Wang Z, Song H, Yu Z-Z, Koratkar N. Enhanced mechanical properties of nanocomposites at low graphene content. ACS Nano 2009;3:3884–90. http://dx.doi.org/10.1021/nn9010472.
[6] Gerson AL, Bruck HA, Hopkins AR, Segal KN. Curing effects of single-wall carbon nanotube reinforcement on mechanical properties of filled epoxy adhesives. Compos Part Appl Sci Manuf 2010;41:729–36. http://dx.doi.org/10.1016/j.compositesa.2010.02.002.
[7] Thess A, Lee R, Nikolaev P, Dai H, Petit P, Robert J, et al. Crystalline ropes of metallic carbon nanotubes. Science 1996;273:483–7. http://dx.doi.org/10.1126/science.273.5274.483.
[8] Ma P-C, Siddiqui NA, Marom G, Kim J-K. Dispersion and functionalization of carbon nanotubes for polymer-based nanocomposites: a review. Compos Part Appl Sci Manuf 2010;41:1345–67. http://dx.doi.org/10.1016/j.compositesa.2010.07.003.
[9] Yazdani H, Hatami K, Khosravi E, Harper K, Grady BP. Strain-sensitive conductivity of carbon black-filled PVC composites subjected to cyclic loading. Carbon 2014;79:393–405. http://dx.doi.org/10.1016/j.carbon.2014.07.082.
[10] Grady BP. Recent developments concerning the dispersion of carbon nanotubes in polymers. Macromol Rapid Commun 2010;31:247–57. http://dx.doi.org/10.1002/marc.200900514.
[11] McNally T, Pötschke P, Halley P, Murphy M, Martin D, Bell SEJ, et al. Polyethylene multiwalled carbon nanotube composites. Polymer 2005;46:8222–32. http://dx.doi.org/10.1016/j.polymer.2005.06.094.
[12] Lapshin RV. Automatic drift elimination in probe microscope images based on techniques of counter-scanning and topography feature recognition. Meas Sci Technol 2007;18:907. http://dx.doi.org/10.1088/0957-0233/18/3/046.
[13] Kovacs JZ, Andresen K, Pauls JR, Garcia CP, Schossig M, Schulte K, et al. Analyzing the quality of carbon nanotube dispersions in polymers using scanning electron microscopy. Carbon 2007;45:1279–88. http://dx.doi.org/10.1016/j.carbon.2007.01.012.
[14] Zhao M, Ming B, Kim J-W, Gibbons LJ, Gu X, Nguyen T, et al. New insights into subsurface imaging of carbon nanotubes in polymer composites via scanning electron microscopy. Nanotechnology 2015;26:085703. http://dx.doi.org/10.1088/0957-4484/26/8/085703.
[15] Wilson SM, Bacic A. Preparation of plant cells for transmission electron microscopy to optimize immunogold labeling of carbohydrate and protein epitopes. Nat Protoc 2012;7:1716–27. http://dx.doi.org/10.1038/nprot.2012.096.
[16] Alig I, Bargmann M, Oehler H, Lellinger D, Wanner M, Koch D. Investigation of delamination mechanisms in polymer coatings by scanning acoustic microscopy. J Phys Appl Phys 2011;44:034009. http://dx.doi.org/10.1088/0022-3727/44/3/034009.
[17] Ivakhnenko V, Eremin Y. Light scattering by needle-type and disk-type particles. J Quant Spectrosc Radiat Transf 2006;100:165–72. http://dx.doi.org/10.1016/j.jqsrt.2005.11.034.
[18] Kashiwagi T, Fagan J, Douglas JF, Yamamoto K, Heckert AN, Leigh SD, et al. Relationship between dispersion metric and properties of PMMA/SWNT nanocomposites. Polymer 2007;48:4855–66. http://dx.doi.org/10.1016/j.polymer.2007.06.015.
[20] Masadome T, Asano Y, Imato T, Ohkubo S, Tobita T, Tabei H, et al. Preparation of refractive index matching polymer film alternative to oil for use in a portable surface-plasmon resonance phenomenon-based chemical sensor method. Anal Bioanal Chem 2002;373:222–6. http://dx.doi.org/10.1007/s00216-002-1329-4.
[21] Nakanishi R, Kitaura R, Warner JH, Yamamoto Y, Arai S, Miyata Y, et al. Thin single-wall BN-nanotubes formed inside carbon nanotubes. Sci Rep 2013:3. http://dx.doi.org/10.1038/srep01385.
[22] Kolmogoroff AN. The logarithmically normal law of distribution of dimensions of particles when broken into small parts. NASA Publication; 1969.
[23] Frømyr TR, Hansen FK, Olsen T. The optimum dispersion of carbon nanotubes for epoxy nanocomposites: evolution of the particle size distribution by ultrasonic treatment. J Nanotechnol 2012;2012:e545930. http://dx.doi.org/10.1155/2012/545930.
[24] Jogi BF, Sawant M, Kulkarni M, Brahmankar PK. Dispersion and performance properties of carbon nanotubes (CNTs) based polymer composites: a review. J Encapsul Adsorpt Sci 2012;02:69–78. http://dx.doi.org/10.4236/jeas.2012.24010.
[25] Shokrieh MM, Saeedi A, Chitsazzadeh M. Mechanical properties of multi-walled carbon nanotube/polyester nanocomposites. J Nanostruct Chem 2013;3:1–5. http://dx.doi.org/10.1186/2193-8865-3-20.
[26] Powell KL, Yeomans JA, Smith PA. Characterization of subsurface damage in ceramic–matrix composites by confocal scanning laser microscopy. J Microsc 1993;169:189–95. http://dx.doi.org/10.1111/j.1365-2818.1993.tb03294.x.
[27] Miyagawa H, Drzal LT. The effect of chemical modification on the fracture toughness of montmorillonite clay/epoxy nanocomposites. J Adhes Sci Technol 2004;18:1571–88. http://dx.doi.org/10.1163/1568561042411204.
[28] Plucknett KP, Pomfret SJ, Normand V, Ferdinando D, Veerman C, Frith WJ, et al. Dynamic experimentation on the confocal laser scanning microscope: application to soft-solid, composite food materials. J Microsc 2001;201:279–90. http://dx.doi.org/10.1046/j.1365-2818.2001.00837.x.
[29] Eftekhari M, Mohammadi S, Khoei AR. Effect of defects on the local shell buckling and post-buckling behavior of single and multi-walled carbon nanotubes. Comput Mater Sci 2013;79:736–44. http://dx.doi.org/10.1016/j.commatsci.2013.07.034.

[30] Yazdani H, Hatami K. Failure criterion for graphene in biaxial loading—a molecular dynamics study. Model Simul Mater Sci Eng 2015;23:065004. http://dx.doi.org/10.1088/0965-0393/23/6/065004.

[31] Koval'chuk AA, Shchegolikhin AN, Shevchenko VG, Nedorezova PM, Klyamkina AN, Aladyshev AM. Synthesis and properties of polypropylene/multiwall carbon nanotube composites. Macromolecules 2008;41:3149–56. http://dx.doi.org/10.1021/ma800297e.

[32] Baughman RH, Zakhidov AA, de Heer WA. Carbon nanotubes–the route toward applications. Science 2002;297:787–92. http://dx.doi.org/10.1126/science.1060928.

[33] Ajayan PM, Schadler LS, Giannaris C, Rubio A. Single-walled carbon nanotube-polymer composites: strength and weakness. Adv Mater 2000;12:750–3. http://dx.doi.org/10.1002/(SICI)1521-4095(200005)12:10<750::AID-ADMA750>3.0.CO;2-6.